Available online at www.sciencedirect.com
ScienceDirect
International Journal of Heat and Mass Transfer 50 (2007) 5269–5282
International Journal of HEAT and MASS TRANSFER
www.elsevier.com/locate/ijhmt

Interfacial thermocapillary pressure of an accelerated droplet in microchannels: Part I. Fluid flow formulation

P.S. Glockner [a], G.F. Naterer [b,*]

[a] Nova 3 Engineering Ltd. 201-120 Fort Street, Winnipeg, Manitoba, Canada R3C 1C7
[b] Faculty of Engineering and Applied Science, University of Ontario Institute of Technology, 2000 Simcoe Street North, Oshawa, Ontario, Canada L1H 7K4

Received 11 August 2006; received in revised form 6 April 2007
Available online 6 August 2007

Abstract

Fluid flow and thermocapillary heat transfer near a droplet/air interface in microchannels is studied analytically and numerically in this set of two companion papers. Thermocapillary forces generate a pressure difference across the droplet, which drives two symmetric re-circulation cells in the upper and lower half-portions of the droplet. The numerical formulation uses a sliding grid for the accelerating droplet, as well as an expanding/contracting grid in the gas region and an adaptive grid in the substrate below the closed-end microchannel. In contrast to past studies with a uniform interfacial pressure, this paper accommodates a varying interfacial pressure along the receding edge of the droplet.

1. Introduction

Effective methods of microfluidic transport have importance in various emerging technologies of micro and nano-systems. Effective flow control improves the thermal performance of micro heat exchangers [1] and microchannel heat sinks for electronics cooling [2]. Past methods of MEMS flow control have used pressure driven [3], electrically driven [4] or thermocapillary driven methods [5]. A comprehensive review of micro-pumping technologies was documented by Singhal et al. [6]. Benefits and limitations of about twenty different types of micro-pumps were described. The maximum flow rates of different micro-pumps were compared. Other comparisons involving actuation voltage, frequency of operation, cost of fabrication and electronics cooling capabilities were reported by the authors [6]. This paper examines a promising alternative to these past methods of flow control, by using thermocapillary forces to generate pressure differences that drive the microfluidic motion.

Thermocapillary forces have been used successfully for flow control along micro-patterned surfaces [7]. Surface micro-grooves have additional benefits of reducing entropy production of convective heat transfer [8]. In a closed-end microchannel, thermocapillary pumping (TCP) involves oscillatory droplet motion during cyclic periods of heating and cooling. Fluid velocities of oscillatory thermocapillary convection have been reported by Agata et al. [9]. Thermocapillary forces have been used to generate pressure gradients across a vapor bubble in a capillary tube [10]. The difference of surface tension across a bubble leads to convective motion towards the region of higher temperature. In nucleate boiling problems, surface tension affects detachment size and departure frequency of bubbles along a surface [11]. Accurate modeling of force and heat balances across bubbles or droplets has importance in various technological problems related to multiphase flows [12–14].

Unlike other conventional methods of flow control in microdevices, thermocapillary control operates without any mechanical moving parts. A miniaturized optical switch involving thermocapillary transport was presented by Togo et al. [15]. Temperature variations within the liquid produce a spatial change of surface tension, thereby

* Corresponding author. Tel.: +1 90517213111; fax: +1 90517213370.
E-mail address: greg.naterer@uoit.ca (G.F. Naterer).

0017-9310/$ - see front matter © 2007 Elsevier Ltd. All rights reserved.
doi:10.1016/j.ijheatmasstransfer.2007.06.018

Nomenclature

A	interfacial area (m^2), surface tension constant
B	surface tension constant
c_p	specific heat (J/kg K)
d	droplet height (m)
F	force (N)
G	microchannel constant
h	convection coefficient (W/m^2 K)
H	microchannel height (m)
k	thermal conductivity (W/m K)
$\dot{m}$	mass flow rate (kg/s)
m	mass of droplet (kg)
M	mass of fluid within control volume (kg)
P	pressure (Pa)
Pe	Peclet number (vH/α)
q''	heat flux (W/m^2)
R	gas constant (J/kg K)
S	source term
t	time (s)
T	temperature (K)
u,v	x and y-velocity components (m/s)
V	volume (m^3)
x, y	Cartesian coordinates (m)

Greek symbols

α	Peclet weighted convection coefficient
β	diffusion coefficient
ϕ	arbitrary scalar value
λ	relaxation coefficient
μ	dynamic viscosity (kg/m s)
θ	contact angle (rad s)
ρ	density (kg/m^3)
σ	surface tension (N/m)

Subscripts

a	air
b	bulk
c	capillary
cl	centerline
d	droplet
e, w, s, n	east, west, south and north integration points
E, W, S, N	east, west, south and north nodal points
f	friction
i	initial
L	left edge
NP, P	neighbouring and central nodes
o	surroundings
R	right edge
s	substrate
v	vertical
w	wall

Superscripts

k	previous iteration
$k+1/2$	current (intermediate) iteration number
n	previous time step
$n+1$	current time step
o	previous iteration or time step
u	velocity

driving microfluidic motion for purposes of pumping or switching. The electrical analogy of this mechanism is electrocapillary transport, whereby an electrical potential gradient between two immiscible conducting fluids generates a spatial change of surface tension. This resulting fluid motion is called continuous electrowetting (CEW). Lee and Kim [16,17] have reported CEW control of a liquid metal droplet in circular microchannels. Unlike CEW, this paper examines how thermal gradients across the fluid can generate fluid motion.

Gurrum et al. [18] used a two-dimensional level set method to predict thermocapillary flow in a microchannel. Variations of surface tension were applied across both ends of the droplet and the predicted results were compared against data obtained from a Poiseuille flow profile. The model predicted a lower average velocity than Poiseuille results, due to the departure of parallel flow in the proximity of the droplet ends. The Poiseuille flow profile represents an approximation for laminar channel flows. Glockner and Naterer [19] have shown that Reichardt's velocity profile can be successfully applied to turbulent channel flows. DeBar and Liepmann [20] manufactured and tested silicon and quartz thermocapillary pumps with a square cross-sectional area. Three heaters were used, with one heater to generate a fluid–vapor interface and two other heaters to control the spatial temperature gradient. The pumps operated under a variety of conditions, in order to evaluate the performance characteristics. These studies considered a square cross-sectional area, while other past studies have investigated other types of geometrical profiles, such as circular microtubes [21], surface microgrooves [22], trapezoidal microchannels [23] and open rectangular microchannels [8]. This paper will examine rectangular microchannel flows, but unlike past papers that considered two open ends of a microchannel, the current study involves closed-ended microchannels with pressurized gas sections at both ends that assist in thermocapillary cycling of the droplet motion.

Sammarco and Burns [24] have described how TCP can be used to pump small volumes of fluid within a micro-fabricated flow channel. TCP velocities up to 20 mm/min were measured for various liquids, with temperature differences ranging from 10 °C to 70 °C. Experiments yielded TCP velocities comparable to theoretical

predictions of the TCP velocity [24]. A subsequent paper by the same authors [25] outlined a thermal analysis of TCP within the microchannel. The analysis investigates both fluid flow and energy transport to develop materials, designs and operational guidelines for effective pumping performance. The interface temperature was reported for droplet velocities less than 0.1 cm/s, when pumping water across a fused silica substrate with a glass microchannel. Thermocapillary forces on detached bubbles in microchannels and fuel cells have been investigated theoretically by Chedester [26]. Non-uniformities of surface tension within the bubble arise from varying temperatures along the surface of the bubble. Thermocapillary forces were shown to distort and elongate bubbles in the direction perpendicular to the heated surface. This distortion augments the drag force, in comparison to partly spherical bubbles with the same volume. The results indicate that thermocapillary forces resist the detachment of bubbles from the wall during the transient process of phase change. In addition to surface tension and drag forces, the current article examines how internal flow recirculation and external pressure forces affect the thermocapillary motion of a fluid in a microchannel.

Thermocapillary forces affect the rate of liquid retention within microscopic surface pores [27]. Yoshida et al. [28] performed a two-dimensional numerical analysis of a micro-pump system driven by surface tension. Gas was trapped between thermoelectric elements interspersed within the channel. The surface force along the interface between the trapped gas and adjacent liquid drove the pump. The thermoelectric elements controlled the magnitude of the surface force. The authors varied certain design parameters of the micro-pump to determine effects of geometrical changes on system performance.

In this article, a 2-D computational fluid dynamics (CFD) model is developed to predict thermocapillary pumping (TCP) in closed-end microchannels. Predictions of TCP within a closed microchannel differ from open microchannels, as pressures upstream and downstream of the droplet are unequal. Large droplet velocities reported in past TCP studies with open-end channels cannot be obtained in a closed-end microchannel, since small droplet displacements create an opposing pressure gradient in the gas region, with a similar magnitude as the thermocapillary pressure. Also, open-end channel assumptions of steady-state Poiseuille flow are not fully applicable in closed microchannels, when cyclic heat input generates periodic acceleration of the droplet. This paper develops a coupled velocity/pressure formulation with a non-uniform interfacial pressure. This interfacial pressure generates thermocapillary forces that drive re-circulating motion near the corners of the droplet. Also, a theoretical model will be developed to predict overall trends arising from different geometrical configurations and thermophysical properties. Comparisons between theoretical and numerical results will be discussed.

2. Thermocapillary pumping in a closed microchannel

Consider a micro-droplet enclosed by air regions on both sides of the droplet within a closed microchannel (see Fig. 1). A stationary heat source is applied at the back end of the droplet, which produces a temperature gradient and thermocapillary force within the droplet. The resulting pressure difference across the droplet generates fluid motion from left to right in Fig. 1. This pressure difference is similar to an externally applied fluid pressure, so certain portions of the flow region exhibit the characteristics of Poiseuille flow. The fluid velocity deviates from Poiseuille flow behavior near the ends of the droplet, due to re-circulation effects. If the interfacial u-velocity along the meniscus is nearly equal to the bulk velocity of the droplet, the shape of the droplet is approximately undistorted.

During thermocapillary pumping, the advancing contact angle is generally different than the receding contact angle during droplet translation. In this paper, the receding and advancing contact angles were both assumed as zero. This approximation is a reasonable assumption when the droplet length is much larger than the channel height, since the volume of the droplet ends becomes small, relative to the total volume of the droplet. It can be shown that the error of the predicted thermocapillary pressure for a water droplet, due to the assumption of a zero contact angle, is about 1.5% for a contact angle of 10°. This deviation could be readily incorporated into the thermocapillary model of the CFD code, provided the contact angles were known. Unfortunately, such data in closed-end microchannels is not available in the archival literature (to our knowledge),

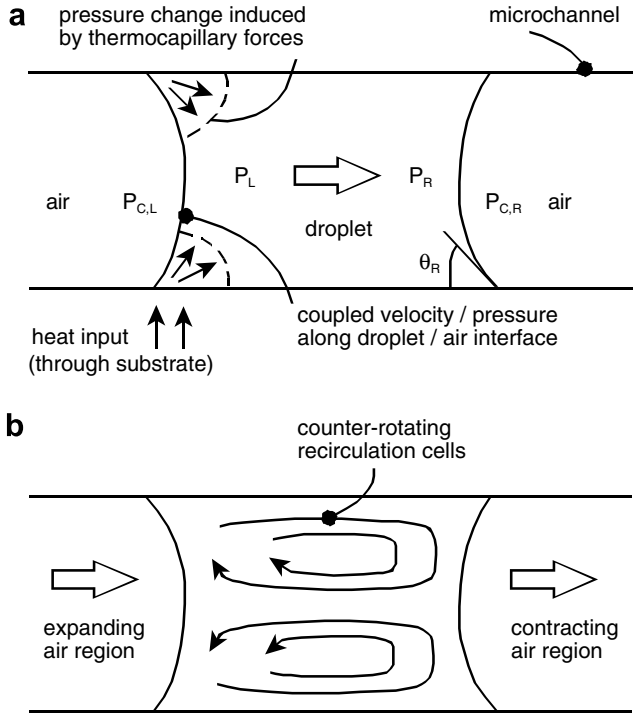

Fig. 1. Schematic of (a) thermocapillary pumping and (b) recirculation cells.

so the current approximation of a zero contact angle was utilized.

The droplet velocity and displacement can be estimated with a slug-flow approximation (SA Model), which treats the droplet as a non-deforming slug. The net force on the droplet consists of a sum of three components, namely: (i) a thermocapillary force (F_c), (ii) external air force (F_a) and (iii) a frictional drag force (F_f). The thermocapillary force is the net force acting on the slug due to the thermocapillary pressure difference [25] (see Fig. 1), i.e.,

$$F_c = \Delta P_c A = (P_{c,R} - P_{c,L})A = GA\left[\left(\frac{\sigma\cos\theta}{H}\right)_R - \left(\frac{\sigma\cos\theta}{H}\right)_L\right] \quad (1)$$

The surface tension at the ends of the droplet depends on temperature, T, as follows,

$$\sigma = A - BT \quad (2)$$

where $A = 75.83$ dyn/cm and $B = 0.1477$ dyn/cm K for water. Also, θ is the contact angle between the liquid and solid and $G = 2(1 + \text{height/width})$ for rectangular microchannels.

An external air force arises from compression or expansion of the gas downstream and upstream of the droplet, respectively. The air surrounding the droplet was treated as a perfect gas according to the ideal gas law, so the external air force on the micro-droplet becomes

$$F_a = \frac{m_a R T_a A}{V_a} \quad (3)$$

where the subscript a refers to air and $R = 0.287$ kJ/kg K for air. It is assumed that liquid in the microchannel stays above the vapor pressure, so that no evaporation occurs and the gas phase remains dry, without moisture added to the air from the liquid.

Also, fluid friction within the droplet is approximated from the following velocity profile corresponding to Poiseuille flow [29],

$$u = -\frac{H^2}{2\mu}\frac{\partial p}{\partial x}\left[\left(\frac{y}{H}\right)^2 - \frac{y}{H}\right] \quad (4)$$

where y is the distance from the channel wall. Based on this velocity profile, the friction force at the wall becomes

$$F_f = \frac{12}{H}\mu\Delta x b u_b = A\Delta P \quad (5)$$

where b and u_b refer to the channel depth and bulk droplet velocity, respectively.

Combining the previous friction, air and thermocapillary forces yields the following net force (F) on the micro-droplet,

$$F = GA\left[\left(\frac{\sigma\cos\theta}{H}\right)_R - \left(\frac{\sigma\cos\theta}{H}\right)_L\right] + AR\left[\left(\frac{m_a T_a}{V_a}\right)_L - \left(\frac{m_a T_a}{V_a}\right)_R\right] + A\Delta P \quad (6)$$

where R, b and ΔP refer to the gas constant (0.287 kJ/kg K for air), microchannel depth and total pressure difference across the droplet, respectively. Based on this net force, the velocity and displacement of the micro-droplet can be determined from temporal integration over a discrete time step, Δt, so that

$$u = u^o + \frac{\Delta t}{m}\left\{GA\left[\left(\frac{\sigma\cos\theta}{H}\right)_R - \left(\frac{\sigma\cos\theta}{H}\right)_L\right] + AR\left[\left(\frac{m_a T_a}{V_a}\right)_L - \left(\frac{m_a T_a}{V_a}\right)_R\right] + A\Delta P\right\} \quad (7)$$

$$x = x^o + u\Delta t \quad (8)$$

These results will be called the analytical SA Model (slug-flow approximation). This theoretical formulation will be used for purposes of comparison and validation against the detailed numerical formulation in the next section.

3. Finite volume formulation of fluid flow

In this section, a numerical method (FVM; finite volume method) is developed to solve the detailed Navier–Stokes equations within the droplet in the closed-end microchannel. The microchannel region, adjoining air regions and surrounding substrate material were sub-divided into discrete control volumes (see Fig. 2). Within each region, the dependent variables are stored at nodal points that are centrally located within the control volumes (see Fig. 3a). The following two-dimensional mass and momentum conservation equations are used to predict the fluid velocities within the micro-droplet.

$$\frac{\partial}{\partial t}(\rho) + \frac{\partial}{\partial x}(\rho u) + \frac{\partial}{\partial y}(\rho v) = 0 \quad (9)$$

$$\frac{\partial}{\partial t}(\rho u) + \frac{\partial}{\partial x}(\rho u u) + \frac{\partial}{\partial y}(\rho v u) = -\frac{\partial p}{\partial x} + \frac{\partial}{\partial x}\left(\mu\frac{\partial u}{\partial x}\right) + \frac{\partial}{\partial y}\left(\mu\frac{\partial u}{\partial y}\right) + \dot{S}_u''' \quad (10)$$

$$\frac{\partial}{\partial t}(\rho v) + \frac{\partial}{\partial x}(\rho u v) + \frac{\partial}{\partial y}(\rho v v) = -\frac{\partial p}{\partial y} + \frac{\partial}{\partial x}\left(\mu\frac{\partial v}{\partial x}\right) + \frac{\partial}{\partial y}\left(\mu\frac{\partial v}{\partial y}\right) + \dot{S}_v''' \quad (11)$$

The algebraic governing equations will be derived after the above Navier–Stokes equations are integrated spatially over the control volumes. Integrating Eq. (9) over a control volume, V, and discrete time step, Δt, it can be shown that the standard finite volume procedure leads to the following result,

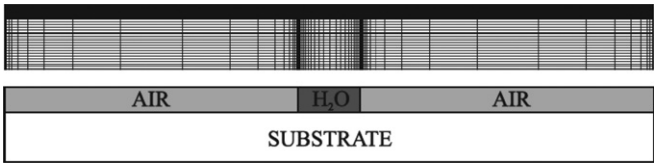

Fig. 2. Schematic of adaptive grid refinement in the closed microchannel.

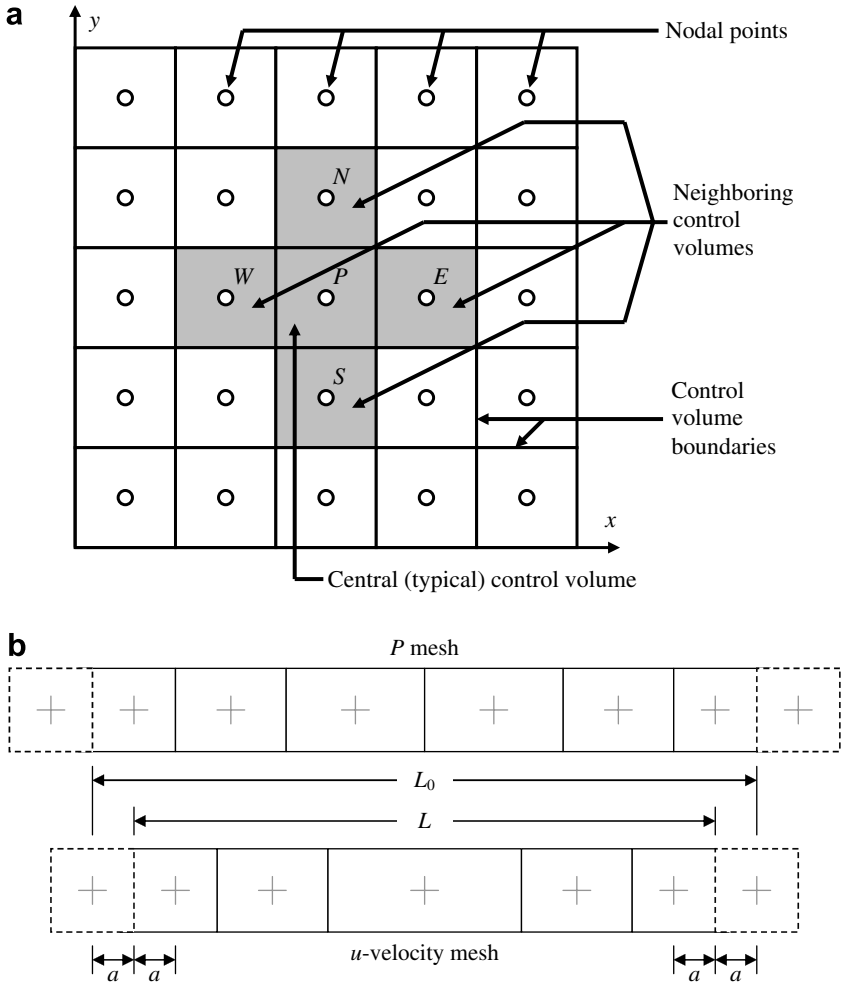

Fig. 3. Schematic of (a) overall grid and (b) pressure/velocity grids.

$$\frac{(M_{\mathrm{P}} - M_{\mathrm{P}}^{n})}{\Delta t} = \dot{m}_{\mathrm{w}} - \dot{m}_{\mathrm{e}} + \dot{m}_{\mathrm{s}} - \dot{m}_{\mathrm{n}} \tag{12}$$

This equation was solved for each control volume within the moving droplet.

A similar discretization is used for the momentum equations. Integrating Eq. (10) over the discrete control volume and time step,

$$\begin{aligned}
&\int_t^{t+\Delta t}\int_V \frac{\partial}{\partial t}(\rho u)\mathrm{d}V\mathrm{d}t + \int_t^{t+\Delta t}\int_V \frac{\partial}{\partial x}(\rho u u)\mathrm{d}V\mathrm{d}t \\
&\quad + \int_t^{t+\Delta t}\int_V \frac{\partial}{\partial y}(\rho v u)\mathrm{d}V\mathrm{d}t \\
&\quad = \int_t^{t+\Delta t}\int_V \frac{\partial}{\partial x}\left(\mu\frac{\partial u}{\partial x}\right)\mathrm{d}V\mathrm{d}t + \int_t^{t+\Delta t}\int_V \frac{\partial}{\partial y}\left(\mu\frac{\partial u}{\partial y}\right)\mathrm{d}V\mathrm{d}t \\
&\qquad + \int_t^{t+\Delta t}\int_V \dot{S}_{\mathrm{u}}'''\mathrm{d}V\mathrm{d}t
\end{aligned} \tag{13}$$

The x-convection term is approximated by

$$\int_t^{t+\Delta t}\int_V \frac{\partial}{\partial x}(\rho u u)\mathrm{d}V\mathrm{d}t \approx \int_t^{t+\Delta t}(\dot{m}_{\mathrm{e}}u_{\mathrm{e}} - \dot{m}_{\mathrm{w}}u_{\mathrm{w}})\mathrm{d}t \tag{14}$$

The integration point velocities can be determined by [30]

$$u_{\mathrm{e}} = \alpha_{\mathrm{e}}u_{\mathrm{P}} + (1-\alpha_{\mathrm{e}})u_{\mathrm{E}} \tag{15}$$

$$u_{\mathrm{w}} = \alpha_{\mathrm{w}}u_{\mathrm{W}} + (1-\alpha_{\mathrm{w}})u_{\mathrm{P}} \tag{16}$$

In these equations, α is a dimensionless coefficient weighted by the local Peclet number (Pe) [30]. This approach represents Peclet weighted upwinding in the convection terms. When calculating advection terms in Eq. (14), the velocity field must be evaluated in the moving droplet's reference frame. The droplet's bulk velocity will be subtracted from the local velocity field, before calculating the advection terms. This procedure involves a moving grid in the droplet, which must stay aligned with the grid points in the substrate. The next section will discuss further details regarding this moving grid formulation.

The diffusion term is approximated as

$$\begin{aligned}
&\int_t^{t+\Delta t}\int_A\int_w^e \frac{\partial}{\partial x}\left(\mu\frac{\partial u}{\partial x}\right)\mathrm{d}x\mathrm{d}A\mathrm{d}t \\
&\quad = \int_t^{t+\Delta t}\left(\mu_{\mathrm{e}}A_{\mathrm{e}}\left.\frac{\partial u}{\partial x}\right|_{\mathrm{e}} - \mu_{\mathrm{w}}A_{\mathrm{w}}\left.\frac{\partial u}{\partial x}\right|_{\mathrm{w}}\right)\mathrm{d}t
\end{aligned} \tag{17}$$

The gradient of u at an interface leading to diffusion is written as

$$\left.\frac{\partial u}{\partial x}\right|_{\mathrm{e}} = \beta_{\mathrm{e}}\frac{(u_{\mathrm{E}}-u_{\mathrm{P}})}{(\Delta x)_{\mathrm{e}}} \tag{18}$$

$$\left.\frac{\partial u}{\partial x}\right|_{\mathrm{w}} = \beta_{\mathrm{w}}\frac{(u_{\mathrm{P}}-u_{\mathrm{W}})}{(\Delta x)_{\mathrm{w}}} \tag{19}$$

where β is a diffusion weighting coefficient that depends on Pe. Combining Eqs. (17)–(19),

$$\int_t^{t+\Delta t}\int_A\int_w^e \frac{\partial}{\partial x}\left(\mu\frac{\partial u}{\partial x}\right)\mathrm{d}x\mathrm{d}A\mathrm{d}t = \left[\left(\frac{\mu_{\mathrm{e}}A_{\mathrm{e}}\beta_{\mathrm{e}}}{(\Delta x)_{\mathrm{e}}}\right)u_{\mathrm{E}} + \left(\frac{\mu_{\mathrm{w}}A_{\mathrm{w}}\beta_{\mathrm{w}}}{(\Delta x)_{\mathrm{w}}}\right)u_{\mathrm{W}} - \left(\frac{\mu_{\mathrm{e}}A_{\mathrm{e}}\beta_{\mathrm{e}}}{(\Delta x)_{\mathrm{e}}}+\frac{\mu_{\mathrm{w}}A_{\mathrm{w}}\beta_{\mathrm{w}}}{(\Delta x)_{w}}\right)u_{\mathrm{P}}\right]\Delta t \tag{20}$$

A similar formulation is used for the y-direction component of diffusion. In these approximations, the dependent variables are assumed to vary linearly between nodal points, so that piecewise linear profiles can be used and variables at a particular node depend only on nearby nodal values. In order to ensure accuracy of linear interpolations used for the above diffusion approximations, various grid refinements were performed until predicted results of droplet displacement and velocity became independent of further grid refinement. After each time step, the velocity mesh is re-generated so that the nodal points within the substrate remain aligned with nodes in the moving droplet. The moving grid procedure will be described in the next section.

The source term arising from thermocapillary forces is sub-divided into a constant portion, S_{c}, and a property dependent portion, S_{P}, i.e.,

$$\int_t^{t+\Delta t}\int_V \dot{S}'''\mathrm{d}V\mathrm{d}t \approx V_{\mathrm{P}}\int_t^{t+\Delta t}(S_{\mathrm{c}}+S_{\mathrm{P}}\phi_{\mathrm{P}})\mathrm{d}t = (Q_{\mathrm{P}}+R_{\mathrm{P}}\phi_{\mathrm{P}})\Delta t \tag{21}$$

where Q_{P} and R_{P} represent the products of the volume and the variables S_{c} and S_{P}, respectively. The source term is linearized with respect to an arbitrary scalar at node p, denoted by ϕ_{p}, which can denote a velocity component or temperature for the momentum or energy equations, respectively.

Assembling all terms and dividing by Δt yields the following x-momentum equation,

$$a^u_{\mathrm{P}}u_{\mathrm{P}} = \sum a^u_{\mathrm{NP}}u_{\mathrm{NP}} + b^u_{\mathrm{P}} \tag{22}$$

where

$$\sum a^u_{\mathrm{NP}}u_{NP} = a^u_{\mathrm{E}}u_{\mathrm{E}} + a^u_{\mathrm{W}}u_{\mathrm{W}} + a^u_{\mathrm{N}}u_{\mathrm{N}} + a^u_{\mathrm{S}}u_{\mathrm{S}} \tag{23}$$

$$a^u_{\mathrm{E}} = \max\left[0,(1-0.1|Pe_{\mathrm{e}}|)^5\right]\frac{\mu_{\mathrm{e}}A_{\mathrm{e}}}{(\Delta x)_{\mathrm{e}}} + \max(-\dot{m}_{\mathrm{e}},0) \tag{24}$$

$$a^u_{\mathrm{W}} = \max\left[0,(1-0.1|Pe_{\mathrm{w}}|)^5\right]\frac{\mu_{\mathrm{w}}A_{\mathrm{w}}}{(\Delta x)_{\mathrm{w}}} + \max(\dot{m}_{\mathrm{w}},0) \tag{25}$$

$$a^u_{\mathrm{N}} = \max\left[0,(1-0.1|Pe_{\mathrm{n}}|)^5\right]\frac{\mu_{\mathrm{n}}A_{\mathrm{n}}}{(\Delta y)_{\mathrm{n}}} + \max(-\dot{m}_{\mathrm{n}},0) \tag{26}$$

$$a^u_{\mathrm{S}} = \max\left[0,(1-0.1|Pe_{\mathrm{s}}|)^5\right]\frac{\mu_{\mathrm{s}}A_{\mathrm{s}}}{(\Delta y)_{\mathrm{s}}} + \max(\dot{m}_{\mathrm{s}},0) \tag{27}$$

$$a^u_{\mathrm{P}} = \frac{M_{\mathrm{P}}}{\Delta t} + a^u_{\mathrm{W}} + a^u_{\mathrm{E}} + a^u_{\mathrm{S}} + a^u_{\mathrm{N}} - R_{\mathrm{P}} \tag{28}$$

$$b^u_{\mathrm{P}} = \frac{M^n_{\mathrm{P}}}{\Delta t}u^n_{\mathrm{P}} + Q_{\mathrm{P}} + \dot{m}_{\mathrm{e}} - \dot{m}_{\mathrm{w}} + \dot{m}_{\mathrm{n}} - \dot{m}_{\mathrm{s}} \tag{29}$$

Eq. (22) is the x-momentum equation and a similar result is obtained for y-momentum.

The coupled mass and momentum equations are solved iteratively by the SIMPLEC procedure (Patankar, [30]), with an iterative line Gauss–Seidel solver on a staggered grid. The staggered grid uses a u-velocity mesh with one fewer column than the pressure mesh (see Fig. 3b). A requirement of the u-velocity mesh is that the centers of the left and right columns of fictitious u-velocity control volumes are located along the left and right edges of the left-most and right-most control volumes, respectively. Grid refinement is performed near the droplet/air interface to improve accuracy of interfacial flux terms.

In the calculation procedure for the interfacial motion, the inlet and outlet boundary conditions for the u-velocity are first calculated. The same value is specified at every node along both menisci to ensure that the droplet remains undistorted. Then, the momentum equations are solved with the current pressure field to obtain new u and v fields. Based on the current temperature field, the new thermocapillary pressure boundary conditions can be specified. Then, the pressure correction equation is solved to obtain the new pressure field, after which the u and v fields are corrected using the new pressure field and the steps are repeated until convergence is reached. In this iterative procedure, both interfacial velocity and pressure fields are initially unknown, but solved iteratively with the coupled momentum equations.

No-slip conditions are applied along the top and bottom walls of the microchannel. At the moving droplet/air interface, the current formulation establishes a non-uniform pressure by solving the interfacial pressure/velocity coupling iteratively with SIMPLEC [30]. The interface velocity is determined iteratively based on the mass flow rate from the previous iteration as follows,

$$u_{\mathrm{bc}} = \frac{\sum_{i=1}^{i_{\max}}\sum_{j=1}^{j_{\max}}u_{i,j}\Delta y_{i,j}}{i_{\max}H} \tag{30}$$

where the subscripts i and j are the row and column numbers, respectively. The updated velocity in Eq. (30) is used as a moving boundary condition for the fluid flow equations, which are solved repeatedly until convergence of the internal flow field is reached.

The pressure field is specified in the control volumes adjacent to the wall at both left and right moving edges of the droplet. Along the upper and lower walls, a no-slip boundary condition is applied to the velocity field. The pressure is specified in all four corners of the droplet, but not the remaining portion of the liquid/air interface. In this

way, the iterative solution of fluid flow equations will allow the pressure and velocity fields to adjust until they satisfy the overall thermocapillary force balance across the droplet. The pressures in the right corners are held at a reference value of zero. Then, the pressure in the left corners is specified in the following manner,

$$P_{\mathrm{L}}^{m+1} = P_{\mathrm{L}}^{m} + \left[\left(\overline{P_{\mathrm{R}}} - \overline{P_{\mathrm{L}}}\right)^{m} - \Delta P_{\mathrm{spec}}\right] \tag{31}$$

where ΔP_{spec} is the sum of the thermocapillary pressure caused by the difference in surface tension across the droplet and the external air pressure difference. This pressure difference induces fluid motion outwards from the corners of the droplet (see Fig. 1). The superscripts m and $m+1$ indicate values at the previous iteration level and the new iteration level, respectively. The average left and right pressures are the weighted averages of the pressures across the left and right boundaries of the droplet, respectively. Upon convergence, the difference in the average pressures will equal the specified pressure difference across the droplet, i.e. $P_{\mathrm{left}}^{\mathrm{m+1}} = P_{\mathrm{left}}^{\mathrm{m}}$.

4. Moving grid procedure

In the previous section, fluid motion was predicted from the solution of the Navier–Stokes equations within the moving droplet. The droplet velocity field is predicted in the reference plane of the overall system. The droplet mesh will move at the droplet's bulk velocity. When viewed in the droplet's reference frame, a re-circulating velocity field will be observed from the numerical results. When solving the governing equations, the momentum grid will slide over a stationary but transient mesh, where the energy equations will be solved (next companion paper). The moving grid will be regenerated at the end of each time step and the temperature field within the substrate will be transformed onto the newly generated mesh. An adaptive grid formulation was developed to accommodate movement of the droplet on a moving grid, relative to the substrate.

The main objective of this paper is presenting the first documented study (to our knowledge) of the non-uniform pressure at the moving droplet/air interface in a microchannel. Past studies have assumed a uniform pressure field, which is decoupled from the re-circulating internal fluid motion and simplified by a Poiseuille flow profile [29]. Since the accuracy of the interfacial flux terms has primary importance in this study, grid refinement was performed near the moving droplet/air interface. The grids were refined in the vicinity of the moving boundary with a Bernstein polynomial. A fifth order polynomial was used in the following form,

$$g(t) = (1-t)^5 P_0 + (1-t)^4 t P_1 + (1-t)^3 t^2 P_2 + (1-t)^2 t^3 P_3 + (1-t) t^4 P_4 + t^5 P_5 \tag{32}$$

where t is a local coordinate bounded by $0 \leqslant t \leqslant 1$. The five P values are the control points that control the expansion ratio of the mesh. The user can specify P_1 with the other control points being calculated as follows,

$$P_0 = 0 \tag{33}$$

$$P_2 = 2P_1 \tag{34}$$

$$P_3 = 1 - P_2 \tag{35}$$

$$P_4 = 1 - P_1 \tag{36}$$

$$P_5 = 1 \tag{37}$$

It is required that

$$0 < P_1 < \frac{1}{4} \tag{38}$$

Assigning a value of $P_1 = 0.2$ yields a uniform mesh. Each of the regions (droplet, surrounding air and substrate in (Fig. 2) may be assigned different values of P_1.

Fig. 3b demonstrates the relation between typical P and u-velocity grids. Examination of the diagram allows us to derive a method for determining the length of the u-velocity mesh, L, based on the existing P mesh. Let the function $g(t)$ represent the Bernstein polynomial of Eq. (32) and let the variable nx represent the number of columns of real control volumes in the P mesh. Then, the following expression for L can be derived as follows,

$$(L_0 - 2a) g\left(\frac{1}{nx-1}\right) = 2a \tag{39}$$

Re-arranging Eq. (39) yields an expression for a in the following form,

$$a = \frac{g L_0/(nx-1)}{2 + 2g/(nx-1)} \tag{40}$$

From Fig. 3b, it can be observed that

$$L = L_0 - 2a \tag{41}$$

Eqs. (40) and (41) are combined to yield the following expression for L.

$$L = \frac{L_0}{1 + g/(nx-1)} \tag{42}$$

In the following section, predicted results from the numerical formulation will be presented.

5. Results and discussion

In this section, three example problems will be presented, namely (i) transient Poiseuille flow in a microchannel (validation problem), (ii) droplet flow in an open-end microchannel (comparison against experimental data) and (iii) droplet flow in a closed-end microchannel (application problem). Problem parameters and thermophysical properties are summarized in Tables 1 and 2 (case 2) and 3 (case 3).

5.1. Case 1: Transient flow in a microchannel with open ends and a closed top surface

The numerical formulation was initially validated through simulation of transient Poiseuille flow in a microchannel. The flow is induced by a suddenly applied pressure gradient at time $t = 0$. Water is enclosed between

Table 1
Thermophysical properties and problem parameters (case 2: $S = 37$)

Property	Value
Channel height (d)	32 μm
Channel depth (b)	500 μm
Droplet length (L)	5276 μm
Receding contact angle (θ_R)	47.6°
Advancing contact angle (θ_A)	49.8°
Minimum temperature difference (ΔT_{min})	19 °C
Geometry constant (S)	37
Dynamic viscosity (μ)	26×10^9 N s/m^2

Table 2
Thermophysical properties and problem parameters (case 2: $S = 12$)

Property	Value
Channel height (d)	50 μm
Channel depth (b)	500 μm
Droplet length (L)	2.5, 12.8, 21 mm
Receding contact angle (θ_R)	39.6°
Advancing contact angle (θ_A)	50.6°
Surface tension hysteresis correction	2.28 cm/s
Geometry constant (S)	12
Dynamic viscosity (μ)	26×10^{-9} N s/m^2

two parallel plates separated by a distance of $H = 30$ microns. Initially ($t = 0$), the liquid is motionless and a constant pressure gradient is then applied across the channel, thereby setting the fluid into motion. The pressure drop across the channel was specified as 1 Pa and the time step size is 0.0001 ms Table 3. The analytical solution for transient developing channel flow is given by

$$u(y,t) = -\frac{H^2}{2\mu}\frac{\partial P}{\partial x}\left\{1 - \left(\frac{y}{H}\right)^2 - \frac{32}{\pi^3}\sum_{k=1}^{\infty}\frac{(-1)^{k+1}}{(2k-1)^3} \times \cos\left[\frac{(2k-1)\pi}{2}\frac{y}{H}\right]\exp\left[-\frac{(2k-1)^2\pi^2}{4H^2}vt\right]\right\} \quad (43)$$

This analytical result will be compared against predicted velocities from the finite volume method (FVM). No-slip conditions along the top and bottom walls and a zero flux along the inlet and outlet faces of the channel were applied for both velocity components. At the channel inlet, the pressure was specified in the wall control volumes as ΔP_{spec}. The length used in the pressure gradient term is the distance between two pressure specification points in the staggered grid.

Table 3
Thermophysical properties and problem parameters

Property	
Density of droplet (ρ)	1000 kg/m^3
Dynamic viscosity (μ)	0.001 kg/m s
Time step (Δt)	0.001 m s
Domain length (L)	30 μm
Channel height (H)	30 μm
Number of x control volumes (nx)	20
Number of x control volumes (ny)	20/80
Pressure difference (ΔP)	1 Pa

Fig. 4 illustrates close agreement between analytical and predicted velocities at different times in the microchannel. The spatial velocity profile is symmetric about the centerline of the microchannel, so only results in a half-portion of the microchannel are depicted. For each time increment of plotted data (0.0002 ms), the fluid velocity in the core of the microchannel increases by about 6.7 μm/s. During this period, the thickness of the boundary layer increases due to transient diffusion of momentum along the wall. The flow becomes fully-developed when boundary layers along each wall merge in the centerline of the microchannel. Such fully-developed conditions are shown in Fig. 5. For both developing flow (Fig. 4) and fully-developed flow in the microchannel (Fig. 5), close agreement between analytical and predicted FVM results is obtained.

The solution error of velocity was calculated at each location and time step as follows,

$$\text{Error} = \frac{u_p - u_a}{u_{a,max}} \quad (44)$$

where u_p and u_a refer to the predicted (FVM) and analytical velocities, respectively. A maximum error of about 8% occurred near the wall in the first time step. This error decreased with each time step and the steady-state results were nearly identical to the analytical solution. The average u-velocity error within the domain was below 0.05% at the steady-state. The steady-state centerline velocity may be calculated in the following manner,

$$u_c = -\frac{H^2}{8\mu}\frac{\partial P}{\partial x} \quad (45)$$

which yields a centerline velocity of 3.75 mm/s. Additional sensitivity results and grid refinement studies were conducted with 20×20 and 20×80 mesh simulations. For both grids, the percentage error was less than about 1% at different locations within the microchannel, so grid-independent results were confidently obtained with the 20×20 mesh discretization.

5.2. Case 2: Microchannel with open ends and open top surface

Sammarco and Burns [24,25] used thermocapillary pumping (TCP) to move nanoliter- and picoliter-sized droplets of liquid within microchannels with open ends and an open top surface. The authors presented the following equation for the steady-state TCP droplet velocity,

$$v = \frac{dGB\cos\theta_R}{LS\mu}(\Delta T - \Delta T_{min}) + \frac{d^2}{S\mu L}(\Delta P_e + \rho g L \sin\phi) \quad (46)$$

where

$$\Delta T = T_R - T_A \quad (47)$$

$$\Delta T_{min} = \left(\frac{A}{B} - T_A\right)\left(1 - \frac{\cos\theta_A}{\cos\theta_R}\right) \quad (48)$$

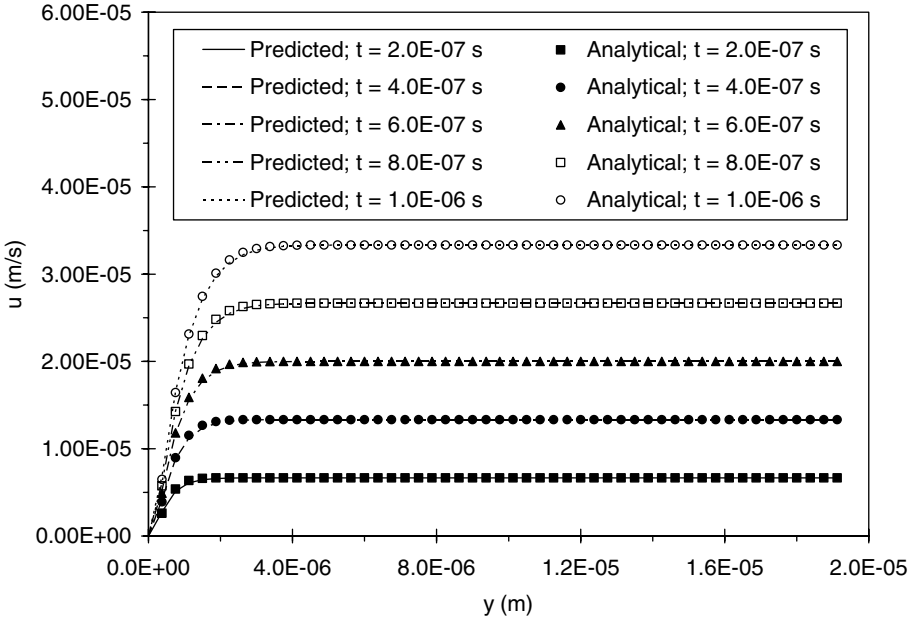

Fig. 4. Predicted velocity profile in a microchannel with open ends (case 1).

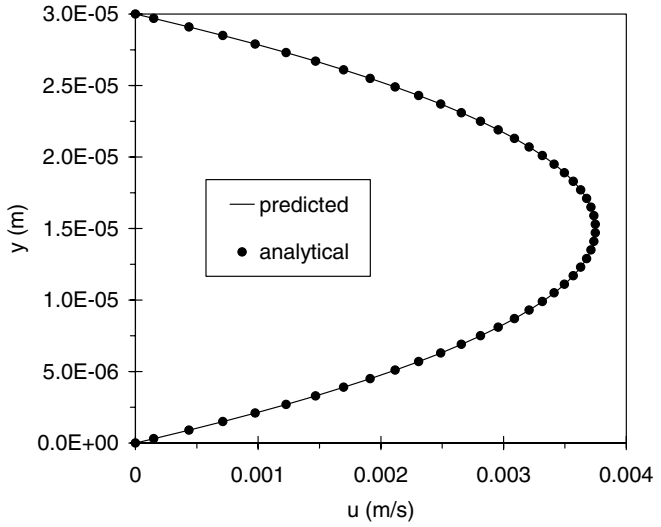

Fig. 5. Steady-state velocity profile in a microchannel.

The variables L, S, $\Delta T_{\min}$, ΔP_e and ϕ are the length of the microdroplet, a geometry-specific constant, minimum temperature difference across the droplet to overcome surface tension hysteresis [24], external (air) pressure difference across the microdroplet and the inclination angle of the microchannel. For the current case of an open-ended microchannel, the external pressures are assumed equal and the microchannel is not inclined.

The microchannels were etched into 500 μm thick wafers using an HNO_3:HF [3:1] etching solution, which yielded a trapezoidal cross-section. Poly-silicon resistive heating elements beneath the microchannels were used to control the droplet motion, while a separate series of poly-silicon resistive temperature detectors was used to measure the temperature field within the microdroplet. The problem parameters are shown in Tables 1 and 2. The values of $\Delta T_{\min} = 19\,^{\circ}\mathrm{C}$ and $S = 37$ used in the numerical simulations were determined experimentally [24] (note: $\Delta T_{\min} = 24\,^{\circ}\mathrm{C}$ seems to better match the experimental data in Ref. [24]).

Rectangular microchannels ($S = 12$) are used in the current numerical simulations, thereby making direct comparisons to experimental data for trapezoidal microchannels difficult. The value of S for trapezoidal microchannels [24] can be determined through a comparison with values of the Poiseuille number, P_0, calculated for similar microchannels by other authors. A geometry coefficient, C_R, can be derived from the Poiseuille number as follows:

$$C_R = \frac{U^2}{8A} P_0 \tag{49}$$

where U is the wetted perimeter and A is the cross-section of the microchannel. The value of C_R may be calculated according to

$$C_R = \frac{12 - 1.38a + 4a^2}{a - 0.85a^2 + 0.28a^3} \tag{50}$$

where

$$a = \frac{\text{height}}{\text{average width}} \tag{51}$$

A channel height of 32 μm and an average channel width of 500 μm yield $a = 0.064$ and a resulting geometry coefficient of $C_R = 196.864$. Rearranging Eq. (54) and solving for the Poiseuille number yields $P_0 = 22.258$. For a trapezoidal microchannel with a height/width ratio of $a = 0.0277$, the Poiseuille number is $P_0 = 22.94$. Also, the Poiseuille number can be written as

$$P_{0,\exp} = \frac{AD_h^2 \Delta P}{2\mu QL} \tag{52}$$

The bulk droplet velocity may be expressed as $u_b = Q/A$, so re-arranging Eq. (52),

$$u_b = \frac{D_h^2 \Delta P}{2\mu L P_{0,\exp}} \tag{53}$$

Alternatively, using the expression derived by Sammarco and Burns [24],

$$u_b = \frac{D^2 \Delta P}{S\mu L} \tag{54}$$

Equating Eqs. (53) and (54), the value of S for the parameters shown in Table 1 becomes 12.6, which is inconsistent with the value of $S = 37$ reported by Sammarco and Burns [24]. It is possible that their microchannel was not a perfect trapezoid, due to manufacturing limitations. The scaling factor S_{num}/S_{exp} used to compare numerical and experimental data in Fig. 6 was $12/37 = 0.32432$.

TCP was studied for various temperature differences of $\Delta T = 8$, 10, 11, 16, 21, 36 and 51 °C in a rectangular microchannel. Eq. (48) yields $\Delta T_{min} = 7.88$ °C. The steady-state bulk droplet velocities corresponding to this minimum temperature difference are labeled as "numerical" in Fig. 6. The curve representing the theoretical steady-state bulk droplet velocities is labeled as "theory" in Fig. 6. The slope of the curves is identical, but the minimum temperature differences required to overcome surface tension hysteresis (corresponding to the intersections of the curves with the x-axis) differ by approximately 2°. It is unclear why the "theory" curve of Sammarco and Burns [24] does not coincide with the results with the value of ΔT_{min} implied by Eq. (48).

Note that substantial uncertainty bars encompassing the discrepancies between theoretical and experimental data were reported by Sammarco and Burns [24]. The authors reported that errors lie with the measurement of advancing and receding contact angles. A measured difference as small as $\theta_A \approx 50 \rightarrow 52°$ and $\theta_R \approx 48 \rightarrow 47°$ shifted ΔT_{min} from about 7 °C to 19 °C [24]. In order to compare the numerical simulations with experimental data corresponding with $\Delta T_{min} = 19$ °C, the "numerical (corrected)" simulations shifted $T_{min} = 19–7.88 = 11.12$ °C along the x-axis. In this case, the shifted velocities in Fig. 6 show good agreement with experimental data. This shifted effect of surface tension hysteresis could be readily incorporated into the numerical simulations, once the values of θ_A and θ_R are known (such as values from experimental data). Good agreement between predicted and experimental data in Fig. 6 provides useful validation of the numerical formulation of thermocapillary pumping over a fixed temperature difference across a droplet in an open-ended microchannel.

Additional validation was performed in Fig. 7 by comparing numerical simulations against experimental data [24] for mineral oil droplets pumped through rectangular microchannels under an applied external pressure gradient. Microdroplets of lengths 2.5 mm, 12.8 mm and 21 mm were considered. The theoretical curve in Fig. 7 is defined by

$$\frac{v}{d/L} = \left(\frac{d}{S\mu}\right)\Delta P_e - \frac{\Delta T_{min} Gb \cos\theta_R}{S\mu} \tag{55}$$

which was derived after dividing Eq. (46) by d/L and setting both ϕ and ΔT to zero. The predicted velocities in the numerical simulations were reduced by 2.28 cm/s, in order to properly account for surface tension hysteresis (second term of Eq. (55)). Experimental uncertainties yield a range of uncertainty. As discussed with Fig. 6, uncertainty bars encompassing the discrepancies between

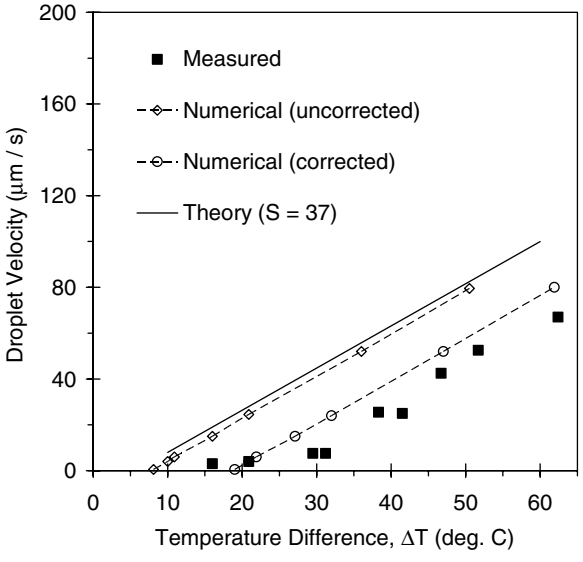

Fig. 6. Droplet velocity in a microchannel with open ends and top surface (case 2).

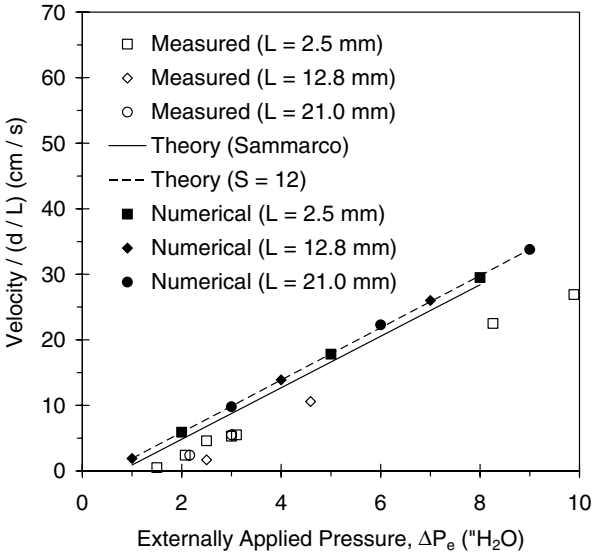

Fig. 7. Droplet velocities at varying pressure differences.

theoretical and experimental data were also reported by Sammarco and Burns [24] for droplet velocities in Fig. 7. The authors reported that the microchannels were not perfectly rectangular, so the value of $S = 12$ yielded poorer agreement with experimental data than actually exists. The slope of the "theory" curve in Fig. 7 closely matches the slope corresponding with experimental data, but the measured velocity increases slower than predictions, when the driving pressure is raised. This discrepancy may have arisen since the dynamic contact angles vary with velocity, whereas the numerical simulations have used constant angles. As discussed previously for Fig. 6, experimental errors with contact angle measurements are believed to be responsible for the deviation between experimental, predicted and theoretical velocities in Fig. 7.

5.3. Case 3: Thermocapillary pumping in a closed-end microchannel

This third problem considers thermocapillary pumping of a discrete droplet in a closed microchannel (see Figs. 1 and 2). Unlike the previous problems, there exists no solution or experimental data in the archival literature for the current problem (to our knowledge). As a result, an approximate model (called the SA Model; slug-flow approximation) will be used for validation purposes. In this problem, the density, viscosity, thermal conductivity and specific heat of the water droplet are 998 kg/m^3, 0.0096 kg/m s, 0.606 W/m K and 4181 J/kg K, respectively. The problem domain includes a water droplet, enclosed air regions and adjoining substrate sections (see Figs. 1 and 2). The droplet length is 100 μm. The density, thermal conductivity and specific heat of the air are 1.16 kg/m^3, 0.0263 W/m K and 1007 J/kg K, respectively, while the property values are 2500 kg/m^3, 0.96 W/m K and 837 J/kg K for the silicon substrate. The initial droplet temperature is 20 °C. Heat is applied to the droplet by bringing a thermal bridge (portion of the substrate composed of a highly conductive material) into contact with a heat source at 30 °C. The microchannel length was 2 mm and a timestep of 0.0005 ms was used in the numerical simulations.

Heat transfer to the receding edge of the droplet produces a thermocapillary force that drives bulk motion of the micro-droplet from left to right in Fig. 1. The current CFD simulations yield both Poiseuille and re-circulating features of the flow field. In Fig. 8, the predicted velocities (relative to the droplet bulk velocity) are shown near the right edge of the droplet. Symmetric re-circulation occurs in the upper and lower halves of the microchannel during bulk movement of the droplet from left to right. In view of problem symmetry, only the lower (or upper) half of the domain needs to be illustrated, with a zero gradient condition along the mid-plane.

In Fig. 8, the fluid decelerates along the midplane as it approaches the right edge, where an adverse pressure gradient re-directs the fluid motion downward along the droplet/air interface and back along the lower microchannel wall. Changes in flow directionality and surface tension in the corners of the micro-droplet affect the onset of re-circulation (at about 9.75 μm in Fig. 8). The droplet deceleration near the corners of the micro-droplet occurs from the combined thermocapillary and friction forces on the micro-droplet, as well as opposing pressures from the compressed and expanded air regions in the end sections of the microchannel (see Fig. 1).

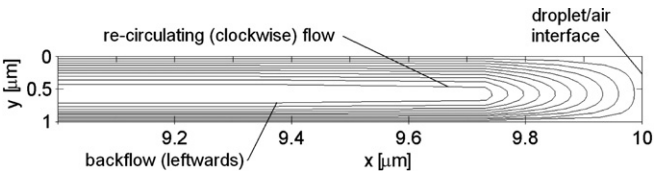

Fig. 8. Streamlines for the relative velocity at the interface for case 3 (note: y measured from the top to the bottom in the upper half of the microchannel).

Fig. 9 shows the pressure distribution along the droplet/air interfaces. The values have been normalized by the average interfacial pressure. Results are plotted at various times during the simulation. It can be observed that the normalized pressure distribution is independent of the time step. This suggests that the pressure distribution reaches a quasi-steady distribution for each time step in the simulation. For sufficiently small droplets and slow heating rates, it appears that the normalized bulk velocity distributions collapse onto a single profile, which depends only on the driving pressure (thermocapillary pressure plus external air pressure).

The bulk velocity is plotted against the instantaneous pressure difference across the channel in Fig. 10. The trend appears to be linear, thereby indicating a direct relationship between the average pressure difference across the droplet and the bulk droplet velocity. This suggests that the bulk droplet velocity can be determined from the

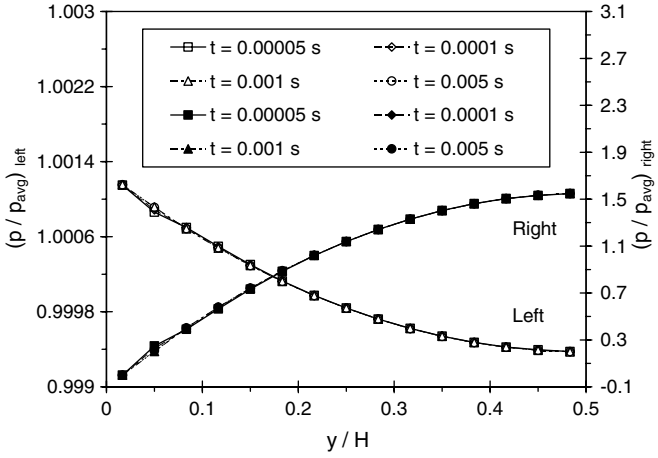

Fig. 9. Normalized pressure distributions at left and right droplet/air interfaces.

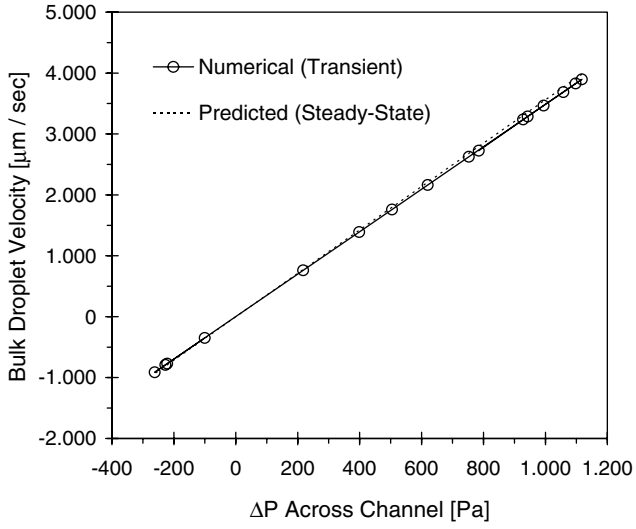

Fig. 10. Predicted transient and steady-state droplet velocities.

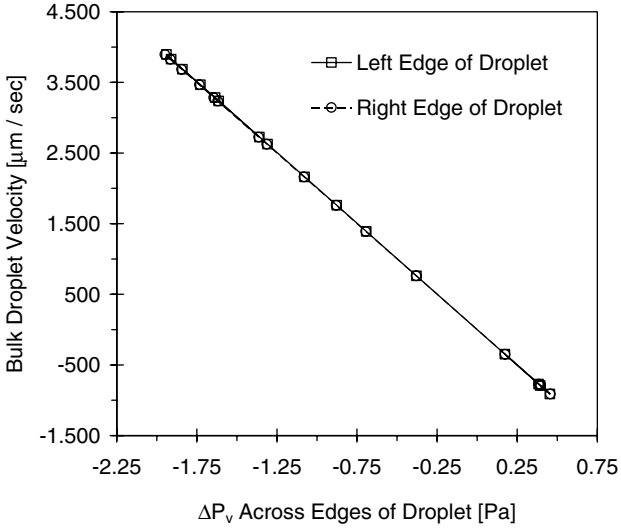

Fig. 11. Pressure differences across droplet/air interface at varying velocities.

steady-state Poiseuille velocity distribution, based on a given pressure difference across the micro-droplet. The expression for the steady-state velocity distribution for laminar Poiseuille flow is [29]

$$u(y) = -\frac{H^2}{2\mu}\frac{\partial P}{\partial x}\left[\left(\frac{y}{H}\right)^2 - \frac{y}{H}\right] \tag{56}$$

where u_b can be determined from

$$u_b = -\frac{H^2}{12\mu\Delta x}\Delta P \tag{57}$$

Eq. (57) is depicted in Fig. 10 as a dashed line. Substituting the problem parameters into Eq. (57) yields an expression of $u_b = -3.5637\Delta P$, where Δx is the distance between the left-most and right-most pressure nodal points (not the length of the droplet). A curve fit of predicted FVM data implies a line with $u_b = -3.4854\Delta P$. Thus, the steady-state assumption over-predicts the bulk droplet velocities by about 2.25% for the given problem parameters. Increasing the droplet mass or magnitude of the heat source would likely magnify this error.

The vertical pressure difference between the channel wall and the channel centerline ($\Delta P_v = P_{cl} - P_w$) along the advancing and receding edges of the droplet is illustrated in Fig. 11. The results show how $(\Delta P_v)_L$ and $(-\Delta P_v)_R$ vary with the bulk velocity of the droplet. The curves appear to be overlapping straight lines. In addition to the pressure profiles scaling directly with the average pressures along the droplet edges (Fig. 9), Fig. 11 indicates that the pressure required to redirect the flow from the channel wall to the centerline varies directly with the bulk droplet velocity.

In Fig. 12, the ratio of the left interfacial pressure to the bulk droplet velocity is shown at various times. It can be observed that the ratio decreases with time, especially between 0.00005 and 0.0001 s, when the droplet accelerates near the beginning of the heating period. Similarly as trends depicted in Fig. 9, the left interfacial pressure rises from the wall inwards to the centerline of the microchannel. This capillary pressure rises over time, while the net pressure difference across the droplet decreases due to the opposing air pressure in the adjoining air region (see Fig. 13). Fig. 13 shows close agreement between numerical and analytical (SA Model) results at early times. The discrepancy rises over time, due to errors with the Poiseuille flow assumption of the SA Model when the droplet decelerates near the end of microchannel.

6. Conclusions

This article has reported new simulation data involving thermocapillary droplet motion in a closed microchannel.

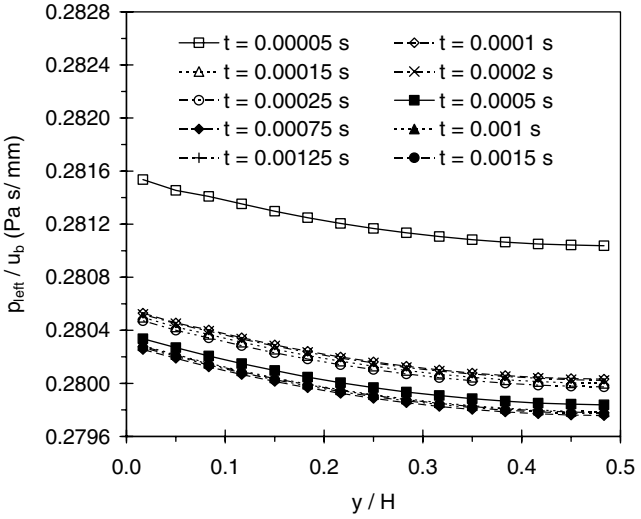

Fig. 12. Pressure/velocity ratio across left edge of droplet/air interface.

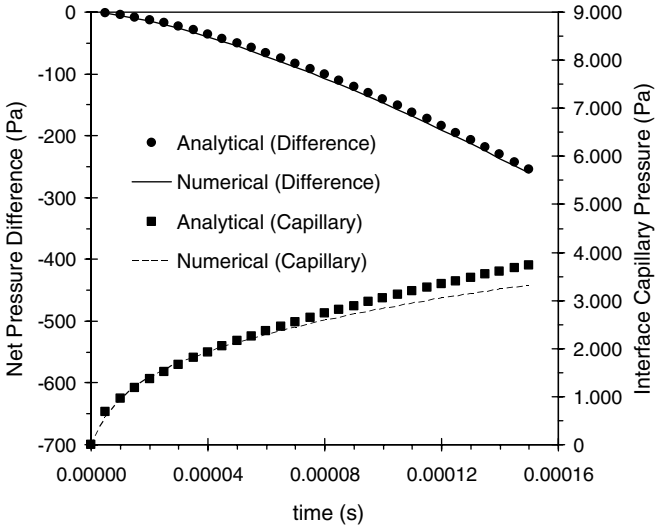

Fig. 13. Predicted capillary pressure (left interface) and net pressure difference across droplet.

A finite volume method with a moving grid was developed to predict the coupled pressure/velocity fields at the droplet/air interface. The implicit pressure/velocity coupling yields new data of fluid re-circulation in the corners of the micro-droplet. This interfacial pressure becomes coupled to the re-circulating velocity field within the micro-droplet. Adaptive mesh refinement is applied at the moving interface with control points to adjust the grid spacing. The predicted results indicate that the external pressure difference across the micro-droplet decreases nearly linearly during the heating period. Predicted data in this paper has provided useful new insight regarding the fluid dynamics of thermocapillary droplet transport in microchannels.

Acknowledgements

Support from the Natural Sciences and Engineering Research Council of Canada, as well as a University of Manitoba Graduate Fellowship (P. Glockner), is gratefully acknowledged.

References

[1] S. Wu, J. Mai, Y.C. Tai, C.M. Ho, Micro heat exchanger using MEMS impinging jets, in: Proceedings of the 12th Annual International Workshop on Micro Electro Mechanical Systems, Orlando, FL, January 17–21, 1999, pp. 171–176.

[2] K. Vafai, L. Zhu, Analysis of a two-layered micro channel heat sink concept in electronic cooling, Int. J. Heat Mass Transf. 42 (1999) 2287–2297.

[3] S. Lim, H. Choi, Optimal shape design of a pressure driven curved micro channel, AIAA Paper 2004-624, AIAA 42nd Aerospace Sciences Meeting and Exhibit, Reno, NV, 2004.

[4] P. Dutta, A. Beskok, T.C. Warburton, Electroosmotic flow control in complex microgeometries, J. Microelectromech. Syst. 11 (1) (2002) 36–44.

[5] C.J. Kim, The use of surface tension for the design of MEMS actuators, in: S.M. Hsu, Z.C. Ying (Eds.), Nanotechnology: Critical Assessment and Research Needs, Kluwer Academic Publishers, Boston, MA, 2003, pp. 239–246.

[6] V. Singhal, S.V. Garimella, A. Raman, Microscale pumping techniques for microchannel cooling systems, Appl. Mech. Rev. 57 (2004) 191–221.

[7] S. Troian, Thermocapillary flow on patterned surfaces: a design concept for microfluidic transport, ASME IMECE Microfluidics Symposium, November, New York, 2001.

[8] G.F. Naterer, Adaptive surface micro-profiling for microfluidic energy conversion, AIAA J. Thermophys. Heat Transf. 18 (4) (2004) 494–501.

[9] Y. Agata, K. Nishino, K. Torii, Characteristics of surface velocity in oscillatory thermocapillary convection, thermal science and engineering, Heat Transf. Soc. Jpn. 11 (4) (2003) 11–13.

[10] N.T. Nguyen, S.T. Wereley, Fundamentals and Applications of Microfluidics, Artech House Publishers, Norwood, MA, 2002.

[11] G.F. Naterer, W. Hendradjit, K.J. Ahn, J.E.S. Venart, Near-wall microlayer evaporation analysis and experimental study of nucleate pool boiling on inclined surfaces, ASME J. Heat Transf. 120 (3) (1998) 641–653.

[12] G.F. Naterer, Reduced flow of a metastable layer at a two-phase limit, AIAA J. 42 (5) (2004) 980–987.

[13] G.F. Naterer, Temperature gradient in the unfrozen liquid layer for multiphase energy balance with incoming droplets, ASME J. Heat Transf. 125 (1) (2003) 186–189.

[14] G.F. Naterer, Heat Transfer in Single and Multiphase Systems, CRC Press, Boca Raton, FL, 2002.

[15] H. Togo, M. Sato, F. Shimokawa, Multi-element thermo-capillary optical switch and sub-nanoliter oil injection for its fabrication, in: Proceedings of the IEEE MEMS Conference, Orlando, FL, 1999, pp. 418–423.

[16] J. Lee, C.J. Kim, Liquid micromotor driven by continuous electrowetting, in: Proceedings of IEEE MEMS Conference, Heidelberg, Germany, 1998, pp. 538–543.

[17] J. Lee, C.J. Kim, Microactuation by continuous electrowetting phenomenon and deep RIE process, in: Proceedings of MEMS Conference, DSC, vol. 66, ASME IMECE Conference, Anaheim, CA, 1998, pp. 475–480.

[18] S. Gurrum, S. Murthyl, Y. Joshi, Numerical simulation of thermocapillary pumping using a level set method, in: Proceedings of the fifth ISHMT/ASME Heat and Mass Transfer Conference, January 3–5, Kolkata, India, 2002.

[19] P.S. Glockner, G.F. Naterer, Near-wall velocity profile with adaptive shape functions for turbulent forced convection, Int. Commun. Heat Mass Transf. 32 (1) (2005) 72–79.

[20] M.J. DeBar, D. Liepmann, Fabrication and performance testing of a steady thermocapillary pump with no moving parts, in: Proceedings of the 15th IEEE International Conference on Micro Electro Mechanical Systems, Las Vegas, NV, 2002, pp. 109–112.

[21] M. Mala, D. Li, Flow characteristics of water through microtubes, Int. J. Heat Fluid Flow 20 (1999) 142–148.

[22] G.F. Naterer, P.S. Glockner, S.R. Chomokovski, G. Richardson, G. Venn, Surface micro-grooves for near-wall exergy and flow control: application to aircraft intake de-icing, J. Micromech. Microeng. 15 (2005) 501–513.

[23] W. Qu, M. Mala, D. Li, Pressure-driven water flows in trapezoidal silicon microchannels, Int. J. Heat Mass Transf. 43 (2000) 353–364.

[24] T.S. Sammarco, M.A. Burns, Thermocapillary pumping of discrete drops in microfabricated analysis devices, AIChE J. 45 (1999) 350–366.

[25] T.S. Sammarco, M.A. Burns, Heat transfer analysis of microfabricated thermocapillary pumping and reaction devices, J. Micromech. Microeng. 10 (2000) 42–55.

[26] C. Chedester, Transport phenomena in microchannels and proton exchange membrane assemblies of fuel cells, M.S. Thesis, George Woodruff School of Mechanical Engineering, Georgia Institute of Technology, Atlanta, Georgia, 2002.
[27] G.R. Schmidt, A. Nadarajah, T.J. Chung, G.R. Karr, Influence of two-phase thermocapillary flow on liquid retention in microscopic pores, Int. J. Multiphas. Flow 22 (1996) 134.
[28] H. Yoshida, M. Saito, H. Toda, R. Haraguchi, Performance analysis on micropump system driven by Marangoni effect, in: Proceedings of the 12th International Heat Transfer Conference, Grenoble, France, August 18–23, 2002.
[29] F.M. White, Fluid Mechanics, Fourth ed., McGraw Hill, 1988.
[30] S.V. Patankar, Numerical Heat Transfer and Fluid Flow, Hemisphere Publishing Corp., 1980.